

Radiometric Degradation Associated with Terrain Height Variations and Pulse Duration in Scan-On-Receive SAR Images

Federica Bordoni, Gerhard Krieger, *Fellow, IEEE*, David Lind

Abstract—Scan-on-receive (SCORE) is a key digital beamforming (DBF) technique for future high-resolution wide-swath spaceborne synthetic aperture radar (SAR) systems. Compared to a conventional approach, it allows to improve the signal-to-noise ratio and the range ambiguity suppression. Nevertheless, it also exposes the system to new errors, associated with terrain height variations and pulse duration. This work investigates the mutual effect of these error sources on the SCORE SAR image. A novel, closed, mathematical expression is derived, respectively, for the impulse response function of the image formation process and for the radiometric loss affecting the image pixels. This makes it possible to predict and quantify the effect of terrain height variations and pulse duration as a function of system, processing, and geometric parameters. The numerical results, based on the end-to-end simulation of the SAR image formation process in different operational scenarios, highlight the relevance of this effect and of the derived analytical description, especially in view of the demanding radiometric quality requirements imposed on future SAR images.

Index Terms— Elevation digital beamforming (DBF), high-resolution wide-swath (HRWS), multichannel synthetic aperture radar (SAR), scan-on-receive (SCORE).

I. INTRODUCTION

SCAN-on-receive (SCORE) [1], [2] is one of the most important digital beamforming (DBF) techniques for forthcoming high-resolution wide-swath (HRWS) spaceborne synthetic aperture radar (SAR) systems [3]–[6]. It plays a key role in the implementation of advanced space-based SAR missions and projects, such as the U.S.-Indian NISAR and Japanese ALOS-4 missions, both scheduled for launch in 2022–2023, the European Copernicus missions ROSE-L and Sentinel-1 Next Generation, and the highly innovative German mission proposal Tandem-L [7]–[11].

According to SCORE, a wide swath is illuminated by using a broad transmit (Tx) beam, whereas, on receive (Rx), multiple digital channels are combined onboard in order to

realize a sharp and high gain elevation beam, that scans the illuminated swath from near to far range, following the pulse echo as it travels along the ground range direction [1], [2]. Compared to a conventional technique, SCORE allows to achieve a higher signal-to-noise ratio and a more efficient suppression of range ambiguities [1], [2]. Nevertheless, a full exploitation of the advantages offered by SCORE-based systems relies on the possibility to properly steer the Rx beam towards the instantaneous direction of arrival (DoA) of the Rx signal.

In the basic SCORE formulation, the Rx beam is steered in real time towards the expected DoA by a simple DBF [1], [2]. This is obtained by summing up the multichannel digital signals, previously multiplied by a range time variant phase. The expected DoA is assumed to be independent of the azimuth time, and to correspond one-to-one with the range time. Specifically, it is computed based on the center of the travelling pulse, a pure spherical Earth model (with no terrain height), and the zero-Doppler geometry. This SCORE solution neglects the pulse duration, the elevation of the backscattering surface, and terrain height variations in the azimuth direction. Accordingly, it works under model mismatch in a real acquisition scenario [12]–[14]. In particular, as illustrated in Fig. 1, due to the pulse duration, the actual instantaneous DoA is given by an angular sector, rather than the expected value [12]. Moreover, the terrain height introduces an offset between actual and expected DoA [13].

The effect of unmodelled terrain height and pulse duration on this basic SCORE technique has been investigated in the literature, both in view of the angular mismatch between actual and expected DoA and the related loss on the Rx power [12]–[14]. However, these effects have been evaluated mainly separately, or without considering the interaction between SCORE DBF and the SAR image processing. As a

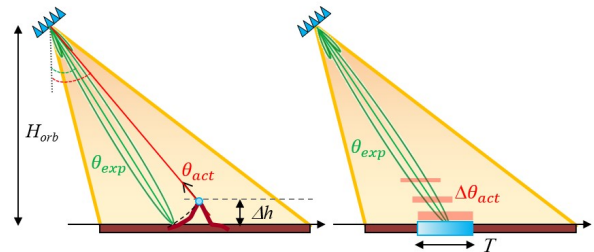


Fig. 1. Zero-Doppler geometry: mismatch between actual and expected DoA, due to unmodelled terrain height (left) and pulse duration (right).

Manuscript received September 2, 2021; revised December 14, 2021, and January 13, 2022; accepted January 25, 2022. Date of current version January 25, 2022.

F. Bordoni, and G. Krieger are with the Microwaves and Radar Institute (IHR), German Aerospace Centre (DLR), 82234 Wessling, Germany (e-mail: federica.bordoni@dlr.de, gerhard.krieger@dlr.de).

D. Lind was with the DLR IHR and the Department of Mathematical Statistics, Lund University, 22362 Lund, Sweden. He is now with Spacemetric AB, SE-191 61 Sollentuna, Sweden (dl@spacemetric.com).

consequence, a prediction of the SCORE SAR image quality degradation, occurring in a real acquisition scenario, is still not possible. This is a relevant drawback, especially considering the demanding requirements on the radiometric quality of future SAR images (accuracy and stability are expected to be below 0.5 dB).

The mentioned basic SCORE technique offers the advantage of a relatively simple and cost-effective implementation. It is conceived for “short pulses” [1], [2], and considered for the realization of systems using pulses with an extension lower than the SCORE beam width [12]. For longer pulses (or sharper beams), already in [1], [2] it was suggested to realize a frequency-dispersive SCORE beam, in order to account for the dependence of the DoA on the pulse components. Different implementations are reported in the literature [1], [2], [15]–[17]. Nevertheless, their successful application in presence of topographic variations has not been addressed yet with sufficient care. In [1], [2], [15], the dispersion is obtained by including in the basic DBF a line of time delays, which implement a phase shift varying linearly over frequency. This solution relies, however, on a pure spherical Earth model and, more specifically, on the assumption of a linear relationship between DoA and range time. Consequently, it may fail in a real acquisition scenario. Especially, fast topographic variations may be critical. More sophisticated solutions are based on the decomposition of the Rx signal into frequency subbands, and the application of specific DBF coefficients to each component [16], [17]. Anyway, in this case too, the compensation of the pulse extension in presence of fast topographic variations may be problematic, due to the constraints imposed by a realistic implementation complexity.

This work investigates the mutual effect of unmodelled terrain height and pulse duration on the SCORE SAR image. The basic SCORE formulation is considered, as a first relevant case of interest. The focus is on the image radiometric quality, with the aim to provide a better understanding of the achievable SAR imaging performance in a real acquisition scenario. Additionally, the impulse response function (IRF) of the image formation process is examined, in order to obtain a more general understanding of the problem. The impact of terrain height and pulse duration is studied from an analytical and numerical perspective; its dependence on acquisition geometry, instrument, and SAR processing parameters is considered too. The investigation is supported by simulations, based on point and distributed target scenarios. Real SAR images, acquired by the TanDEM-X mission [18], are also used to generate the SCORE SAR image. Initial results, already published in a short conference paper [19] and a master thesis [20], are here extended, further justified and discussed.

The paper is structured as follows. Section II describes the data model and presents the problem to solve. Sections III–VI investigate the effect of terrain height variations and pulse duration from an analytical perspective: the transfer function of the SCORE SAR image formation process is derived in Section III; the SCORE IRF is analyzed in Section IV; a closed expression of the SAR image radiometric degradation is derived in Section V; Section VI extends the previous results by considering the effect of a SAR Rx window. The

numerical analysis, based on the end-to-end simulation of the SAR image formation process in different acquisition scenarios, is reported in Section VII, followed by the concluding remarks in Section VIII. Appendices A and B provide mathematical details on the obtained results.

II. DATA MODEL AND PROBLEM STATEMENT

Let us consider a DBF SAR system with SCORE capability. The architecture is based on a planar array antenna with K digital Rx elevation channels, uniformly distributed along the antenna height, h_{ant} . Without loss of generality, the array element spacing, $d = h_{ant}/K$, is assumed small enough to allow approximating the antenna elevation Rx pattern by the array factor (AF) [21]:

$$AF(\theta) = \sum_{k=1}^K \exp \left\{ j \frac{2\pi d (k - 0.5 - 0.5K) \sin(\theta - \theta_{ilt})}{\lambda} \right\} \approx K \operatorname{sinc} \left\{ \frac{h_{ant} \sin(\bar{\theta})}{\lambda} \right\}, \quad (1)$$

where θ denotes the elevation angle measured w.r.t. nadir in the zero-Doppler plane, i.e., the look angle; θ_{ilt} the antenna tilt angle, set such that the boresight direction intersects the imaged swath; $\bar{\theta} = \theta - \theta_{ilt}$; λ the radar wavelength¹; j the imaginary unit. Let us assume, for the sake of simplicity, that the data are acquired in stripmap mode (coupled with SCORE), and neglect the effect of the range cell migration (RCM)² [14], [22].

Based on the previous assumptions, SCORE behavior can be investigated by considering only the zero-Doppler geometry (Fig. 1) and the one-dimensional SAR processing in range [13]. In particular, the relevant SAR image formation process is represented by the block diagram in Fig. 2, with reference to the discretized baseband signals. As shown in the figure, a generic range line of the simulated SCORE SAR image is obtained from the reflectivity function and the actual terrain height of the corresponding surface stripe.

More in detail, the imaged surface stripe is modelled as a discrete sequence of scatterers, positioned along the range direction, and spaced by the range sampling interval, assumed to be (approximately) equal to the range resolution cell size. The backscattered signal is then described by the ground reflectivity function, $g(t)$, being t the discretized range time (two-way time delay). For instance, the reflectivity is a Dirac delta for a point target, such as a corner reflector; for a distributed uniform target, such as a homogeneous forest, it is

¹ The radar wavelength is assumed to be constant, and given by the value associated with the carrier frequency. A more accurate model could include the antenna pattern dependence on the operational frequency [14]. Nevertheless, the analysis of this effect goes beyond the aims of the present work.

² It is worth to remark that, in first approximation, the reported analysis applies in presence of RCM too, even if the effect of the RCM on the SCORE DBF and SAR image formation process is assumed to be negligible. In fact, for typical HRWS spaceborne SAR system parameter values, the samples received from a point target, in each range sweep during the azimuth integration time, are weighted approximately by the same SCORE pattern values [14], [22]. Accordingly, the RCM effect on the SAR image formation process can be compensated in a conventional way.

a stationary white complex Gaussian (WCG) random process³, with zero mean and mean power, given by the “radar cross section” of the resolution cell [21], [23].

According to the actual topographic profile in the vertical, zero-Doppler plane (Fig. 1), each reflectivity sample is associated with an actual DoA⁴, $\theta_{act}(t)$, and a set of interferometric phases at the antenna Rx channels,

$$\phi_k(t) = \frac{2\pi d (k - 0.5 - 0.5K) \sin[\bar{\theta}_{act}(t)]}{\lambda}, \quad k=1, \dots, K, \quad (2)$$

where $\phi_k(t)$ is measured w.r.t. the center of the array of elevation channels; $\bar{\theta}_{act} = \theta_{act} - \theta_{ilt}$; t is the range time of the considered reflectivity sample.

The useful signal, received by each channel, can then be described as the convolution of the transmitted chirp pulse, $c(t)$, with the reflectivity, previously multiplied by the corresponding interferometric phase:

$$r_k(t) = [g(t) e^{j\phi_k(t)}] \otimes c(t), \quad k=1, \dots, K, \quad (3)$$

where \otimes denotes the convolution operator, and $g(t) e^{j\phi_k(t)}$ the reflectivity “seen” by each channel.

SCORE DBF is applied to this set of K raw data, by including a range time dependent phase excitation,

$$\psi_k(t) = -\frac{2\pi d (k - 0.5 - 0.5K) \sin[\bar{\theta}_{exp}(t)]}{\lambda}, \quad (4)$$

and adding up the K signals:

$$s(t) = \sum_{k=1}^K r_k(t) e^{j\psi_k(t)}, \quad (5)$$

where $\theta_{exp}(t) = \bar{\theta}_{exp}(t) + \theta_{ilt}$ denotes the expected DoA, assumed to correspond one-to-one with the range time.

As a result, the antenna Rx beam is steered in real time towards the expected DoA. In particular, from (1), the SCORE pattern is given by

$$AF(\theta_{exp}(t), \theta) \approx K \text{sinc} \left\{ \frac{h_{ant}}{\lambda} [\sin(\bar{\theta}) - \sin(\bar{\theta}_{exp}(t))] \right\}. \quad (6)$$

It is worth to remark that the SCORE steering law, $\theta_{exp}(t)$, does not depend on the azimuth time, i.e., the same steering is applied in each range sweep during the whole SAR acquisition [1], [2]. In contrast to this, the relationship between actual DoA and range time, $\theta_{act}(t)$, changes in general from sweep to sweep, due to the terrain height variations.

Finally, the range compression is applied by the matched filter, to obtain a range line of the simulated SCORE SAR image:

$$q(t) = s(t) \otimes c^*(-t). \quad (7)$$

As a comparison, Fig. 3 shows the relevant SAR image formation process for a conventional (single Rx channel)

³ The reflectivity samples can be assumed: (i) independent, since originated by different areas; (ii) CG, due to the Central Limit theorem; (iii) identical distributed, since the backscattering scene is homogeneous [21]. More in general, for a heterogeneous natural scene, the point (i) and (ii) generally still apply; for an anthropogenic surface, they may not hold [21].

⁴ For sake of simplicity, in the present analysis, layover and shadow are not considered, i.e., a one-to-one relationship between reflectivity sample, range time, and actual DoA is assumed.

system. Here the SAR processing reduces to the range compression of the signal received by a single channel [23]:

$$q_c(t) = r(t) \otimes c^*(-t). \quad (8)$$

Let us now discuss more in detail the SCORE steering law [1], [2]. The SCORE steering direction, $\theta_{exp}(t)$, is assumed to have a one-to-one correspondence with the range time, and to be independent of the azimuth time. It is computed with reference to the zero-Doppler geometry, based on the position of the center of the backscattering pulse and a simple reference topographic profile. For instance, the reference topographic profile generally used to describe SCORE and predict the system imaging performance is that of a spherical Earth with no terrain elevation.

This basic SCORE formulation has the advantage of a relatively simple implementation, and is considered for SAR systems transmitting pulses with an extension smaller than the half power beam width (HPBW) of the SCORE pattern. However, pulse duration and unmodelled terrain height generate a mismatch between actual and expected DoA. In particular, the pulse duration, T , is associated with a twofold error: for a distributed target, the actual DoA is an angular sector (Fig. 1, right) [1], [2], [12]; for a point target, the actual DoA is constant vs. range time for the whole pulse duration [14]. As regards the unmodelled terrain height, Δh , it introduces an offset between the actual DoA of the center of the pulse and the expected one (Fig. 1, left) [13]. Note that this topographic error may occur independently of the reference topographic profile used to compute the expected DoA. In fact, since the SCORE steering does not depend on the azimuth time, errors associated with terrain height variations in the azimuth directions may be unavoidable.

The two steering errors are plotted in Figs. 4 and 5, as a function of the acquisition geometry [14]. As shown in the figures, the errors are larger in near range, and for lower orbit heights: around 20 deg incidence angle, for an orbit height of 500 km, the errors due to topography and pulse duration could

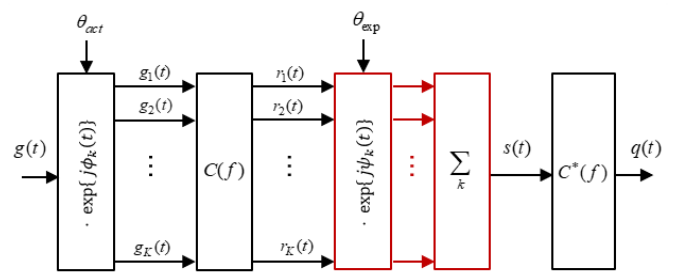


Fig. 2. SCORE-based SAR system (K digital Rx channels): block diagram of the relevant SAR image formation process, from the ground reflectivity of the imaged scene to (a range line of) the final SAR image. The first two blocks represent the raw data acquisition; the next two (in red) SCORE DBF; the last one the range compression by a matched filter. All signals are in baseband and discretized.

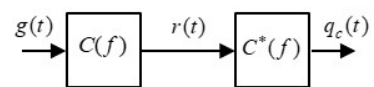


Fig. 3. Conventional SAR system: block diagram of the relevant SAR image formation process. The first block represents the raw data acquisition; the last one the range compression. All signals are in baseband and discretized.

reach values around 0.6 deg and 1.2 deg, respectively.

The mutual effect of pulse duration and topography on the Rx power is described in the literature by the so-called pulse extension loss (PEL) [12]:

$$PEL(\theta_{\text{exp}}) = \frac{\int |R_s(\theta_{\text{exp}}, \theta)|^2 d\theta}{\Delta\theta_{\text{act}}(\theta, h)}, \quad (9)$$

where θ denotes the elevation angle; $R_s(\theta_{\text{exp}}, \theta)$ the value in θ of the normalized SCORE pattern, steered towards θ_{exp} ; $\Delta\theta_{\text{act}}$ the pulse extension (i.e., the width of the angular sector associated with the footprint on ground of the pulse), computed according to the actual terrain height, h . However, the PEL cannot be used to predict the radiometric loss on the SAR image. In fact, it quantifies in general only the power loss on the SAR raw data, under the assumption of a homogeneous backscattering surface.

The problem of interest is to clarify the mutual effect of pulse duration and unexpected terrain height on the SAR imaging performance of SCORE-based systems. With this aim, the IRF of the image formation process is derived and analyzed. Moreover, in order to quantify the radiometric degradation at image level, the following figure of merit, denoted as SCORE loss (SL) for a distributed target, is defined and studied:

$$SL_d(t_0) = \frac{P(t_0)}{K^2 P_c(t_0)} = \frac{E\{|q(t_0)|^2\}}{K^2 E\{|q_c(t_0)|^2\}}, \quad (10)$$

where $P(t_0)$ is the mean power of a pixel in the SAR image, obtained by SCORE; $P_c(t_0)$ the mean power of the same pixel, obtained by conventionally processing a single channel; t_0 the pixel position, in range time; $E\{\cdot\}$ the expectation operator.

III. EQUIVALENT LINEAR TIME-VARYING FILTER

Let us consider the SAR image formation process of a SCORE-based system in Fig. 2 for a point target. The input ground reflectivity function is given by

$$g(t) = \mu \delta(t - t_0), \quad (11)$$

where t_0 denotes the range time of the target; μ a complex amplitude, assumed equal to one in the following without loss of generality.

The discretized baseband Rx signal at the k -th digital elevation channel (neglecting a complex scaling factor) can be written as [15]

$$r_k(t) = c(t - t_0) \exp\{j\phi_k(t_0)\}, \quad (12)$$

where $\phi_k(t_0)$ denotes the interferometric phase in (2), associated with the actual DoA, $\theta_{\text{act}}(t_0)$, of the target; and

$$c(t) = \text{rect}\left(\frac{t}{T}\right) \exp\{j\pi K_r t^2\} \quad (13)$$

the Tx chirp; being T the chirp duration, and K_r the chirp rate. The range sampling frequency, S_f , is approximately

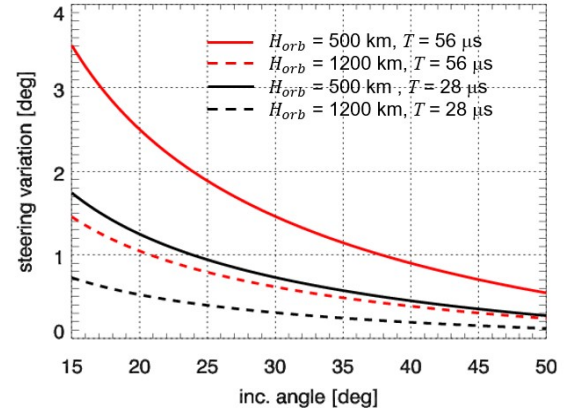


Fig. 4. Zero-Doppler geometry: SCORE steering variation during a time interval equal to the pulse duration vs. incidence angle, for different values of orbit heights, H_{orb} , and pulse duration, T . The SCORE steering law is assumed to be based on a spherical Earth model, with no terrain height. The maximum steering error due to the pulse duration is about half the steering variation.

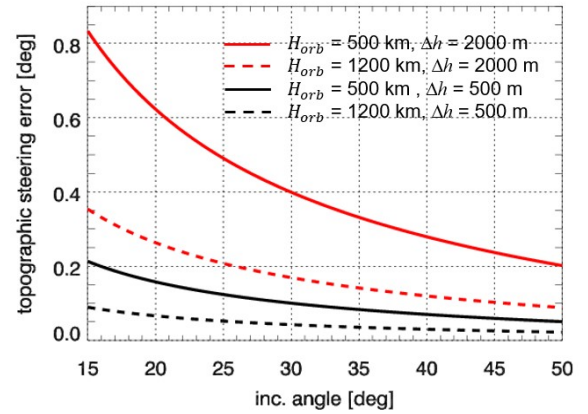


Fig. 5. Zero-Doppler geometry: steering error due to unmodelled terrain elevation, Δh , vs. incidence angle, for different H_{orb} . The SCORE steering law is assumed to be based on a spherical Earth model, with no terrain height.

equal to the chirp bandwidth, $B_c = |K_r T|$. Note that $\phi_k(t_0)$ is constant w.r.t. range time, t .

SCORE DBF is applied to the set of K received signals⁵:

$$\begin{aligned} s(t) &= \sum_{k=1}^K r_k(t) \exp\{j\psi_k(t)\} = \\ &= c(t - t_0) AF(\theta_{\text{exp}}(t), \theta_{\text{act}}(t_0)), \end{aligned} \quad (14)$$

where the last equivalence is obtained from (1) and (6).

Equation (14) shows that SCORE DBF behaves like a window, weighting the samples received from a point target in t_0 by the values of the SCORE pattern:

$$w_{AF}(t, t_0) = AF(\theta_{\text{exp}}(t), \theta_{\text{act}}(t_0)), \quad |t - t_0| \leq T/2, \quad (15)$$

⁵ A first attempt to describe the Rx signal modulation was given in [12], by considering the signal instantaneously received from a distributed target. This should anyway not be confused with the modulation of the signal received from a point target in (14), which is necessary to characterize the IRF of the SAR image formation process.

where $AF(\theta_{\exp}(t), \theta_{act}(t_0))$ denotes the array factor, i.e., the SCORE Rx pattern, steered towards $\theta_{\exp}(t)$ and computed in $\theta_{act}(t_0)$. In fact, each sample received from the target with DoA, $\theta_{act}(t_0)$, during the pulse duration, is weighted by a different SCORE pattern value, according to the SCORE steering law, $\theta_{\exp}(t)$.

It is useful to remark that, for the considered planar array, $AF(\theta_1, \theta_2) = AF(\theta_2, \theta_1)$ and the window in (15) can be equivalently expressed by the SCORE pattern steered towards $\theta_{act}(t_0)$ and computed in $\theta_{\exp}(t)$:

$$w_{AF}(t, t_0) = AF(\theta_{act}(t_0), \theta_{\exp}(t)), \quad |t - t_0| \leq T/2. \quad (16)$$

This expression of w_{AF} allows a direct visualization of the SCORE pattern sector weighting the received samples.

Finally, the convolution with the matched filter returns the IRF, $h_s(t, t_0)$. Accordingly, the overall transfer function of the image formation process is

$$H_s(f, t_0) = FT\{h_s(t, t_0)\} = C(f) W_{AF}(f, t_0) C^*(f), \quad (17)$$

where $C(f)$ denotes the discrete-time Fourier transform (FT) of $c(t)$; $(\cdot)^*$ the complex conjugate operator; and

$$W_{AF}(f, t_0) = w_{AF}(t, t_0)|_{t=f/K_r}, \quad (18)$$

is the expression in the frequency domain of the window w_{AF} , obtained by means of the one-to-one correspondence between frequency and time for the linear FM chirp pulse.

As shown by (17), $H_s(f, t_0)$ is composed of three factors: the first and last one describe the conventional process (convolution of the ground reflectivity with the Tx chirp, and range compression by matched filter); the middle one SCORE DBF. The related block diagram is displayed in Fig. 6.

Equation (17) provides a novel representation of the SCORE image formation process as a linear time-varying (LTV) filter, equivalent to that in Fig. 2 as regards input and output.

Concerning the effect of unmodelled terrain height variations and pulse duration, the previous derivation shows that they do not affect the image formation process, if two conditions are simultaneously satisfied:

- (i) $\theta_{\exp}(t_0) \approx \theta_{act}(t_0)$;
- (ii) $|\theta_{\exp}(t) - \theta_{act}(t_0)| \ll \text{HPBW}$, for $|t - t_0| \leq T/2$,

where HPBW denotes the half power beam width of SCORE Rx pattern, approximately equal to $0.89\lambda/h_{ant}$ for the considered planar system [21]. The first condition means that the assumed reference topographic profile reflects the actual one; the second that the pulse duration is negligible. In this *ideal case*, all the samples received from the point target are weighted by a constant AF equal to K , and SCORE DBF just amplifies the conventional SAR signal by a factor K , i.e.,

$$H_s(f) = K |C(f)|^2. \quad (19)$$

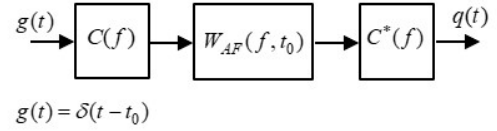


Fig. 6. SCORE-based SAR system: block diagram of the equivalent SAR image formation process, for a target at t_0 .

In a more realistic case, where a mismatch between expected and actual DoA is present, the received samples are weighted by $AF(\theta_{\exp}(t), \theta_{act}(t_0))$, with $|AF(\theta_{\exp}(t), \theta_{act}(t_0))| \leq K$.

Note that, for a very short pulse, all the Rx samples are weighted (approximately) by $AF(\theta_{\exp}(t_0), \theta_{act}(t_0))$, i.e.,

$$H_s(f) \approx AF(\theta_{\exp}(t_0), \theta_{act}(t_0)) |C(f)|^2, \quad (20)$$

and $\theta_{act}(t_0) - \theta_{\exp}(t_0)$ is the topographic steering error (Fig. 5).

IV. IMPULSE RESPONSE FUNCTION ANALYSIS

Equations (17) and (19) show that in SCORE-based SAR systems, unmodelled terrain height variations and pulse duration affect the image formation process. In order to describe their effect on the IRF, it is worth to note that $W_{AF}(f, t_0)$ is a real function without a specific symmetry,

whereas $|C(f)|^2$ is symmetric with respect to the central frequency of the pulse, $f_0 = K_r t_0$. Accordingly, the IRF is not real and symmetric w.r.t. t_0 , as in the ideal (and conventional) case, but complex with symmetric amplitude and antisymmetric phase.

Concerning the radiometric properties, since $|W_{AF}(f, t_0)| \leq K$, the IRF peak power and energy values reduce compared to the ideal ones. In particular, from (14), the value of the IRF at the target location is

$$\begin{aligned} q(t_0) &= \sum_t |c(t - t_0)|^2 AF(\theta_{\exp}(t), \theta_{act}(t_0)) = \\ &= \sum_{t=t_0-T/2}^{t_0+T/2} AF(\theta_{\exp}(t), \theta_{act}(t_0)) = \sum_{t=t_0-T/2}^{t_0+T/2} w_{AF}(t, t_0). \end{aligned} \quad (21)$$

In the ideal case $q(t_0) = K N_s$, being $N_s = T S_f$ the number of integrated pulses. Then, the SCORE loss on the IRF peak power is given by

$$SL_p(t_0) = \frac{|q(t_0)|^2}{(K N_s)^2} = \frac{\left| \sum_{t=t_0-T/2}^{t_0+T/2} AF_n(\theta_{\exp}(t), \theta_{act}(t_0)) \right|^2}{N_s^2}, \quad (22)$$

where $AF_n = AF/K$ denotes the normalized AF.

As regards the energy of the IRF, the loss is given by

$$\begin{aligned} SL_e(t_0) &= \frac{\sum_t |h_s(t, t_0)|^2}{K^2 \sum_t |c(t) \otimes c^*(-t)|^2} = \frac{\int |H_s(f, t_0)|^2 df}{K^2 \int |C(f)|^4 df} = \\ &= \frac{\int |C(f) W_{AF}(f, t_0)|^2 df}{K^2 \int |C(f)|^2 df} = \frac{\sum_t |c(t - t_0) w_{AF}(t, t_0)|^2}{K^2 \sum_t |c(t)|^2} = \end{aligned}$$

$$= \frac{\sum_{t=t_0-T/2}^{t_0+T/2} \left| AF_n(\theta_{\text{exp}}(t), \theta_{\text{act}}(t_0)) \right|^2}{N_s}, \quad (23)$$

where the equivalences descend from the Parseval's theorem, the fact that $|C(f)|$ is (approximately) constant over the chirp bandwidth and $|c(t)| = 1$ [24], [25].

The pattern values in (22) and (23) are the same as in the SCORE pattern window, $w_{AF}(t, t_0)$, in (15). Indeed, according to (23), the IRF energy loss is given by the ratio between the energy of a chirp weighted by the SCORE pattern window and that of a chirp weighted by a rectangular window with magnitude K .

It is worth to note that for a very short pulse, the loss depends only on the topographic error and is given by

$$SL_p(t_0) = SL_e(t_0) = \left| AF_n(\theta_{\text{exp}}(t_0), \theta_{\text{act}}(t_0)) \right|^2. \quad (24)$$

As regards the phase of the IRF, as mentioned, it is in general antisymmetric w.r.t. t_0 , and depends mutually on $\theta_{\text{act}}(t_0)$ and $\theta_{\text{exp}}(t)$ through the SCORE pattern shape. However, it can be easily derived from Section III that the interferometric phase obtained from IRFs of SCORE-based systems is equal to the conventional one, as long as the SCORE pattern and the actual DoA, $\theta_{\text{act}}(t_0)$, are the same for the combined SCORE SAR images.

V. SAR IMAGE RADIOMETRIC DEGRADATION

In case of a distributed target, the radiometric degradation at SAR image level is quantified by the SCORE loss in (10), as the pixel mean intensity reduction w.r.t. the ideal case. In particular, under the assumption that the reflectivity samples can be modelled as independent, random, variables with zero mean, it is given by (see Appendix A)

$$SL_d(t_0) = SL_e(t_0) = \frac{\sum_{t=t_0-T/2}^{t_0+T/2} \left| AF_n(\theta_{\text{exp}}(t), \theta_{\text{act}}(t_0)) \right|^2}{N_s}, \quad (25)$$

where t_0 here is the range time of the considered pixel, and $\theta_{\text{act}}(t_0)$ the actual DoA of the corresponding imaged area (resolution cell).

Equation (25) is generally valid for natural imaged surfaces. If the samples of the ground reflectivity are not independent, but the reflectivity is stationary with zero mean, the SL can be obtained from (17)-(19) [24]:

$$\begin{aligned} SL_d(t_0) &= \frac{\int S_g(f) |H_s(f, t_0)|^2 df}{K^2 \int S_g(f) |C(f)|^4 df} = \\ &= \frac{\int_{B_c} S_g(f) |W_{AF}(f, t_0)|^2 df}{K^2 \int_{B_c} S_g(f) df}, \end{aligned} \quad (26)$$

where $S_g(f)$ denotes the power spectral density (PSD) of the ground reflectivity; B_c the chirp bandwidth.

The derived expression of the SL quantifies the radiometric degradation at SAR image level, as a function of the actual topography, the pulse duration, the acquisition geometry, the SCORE pattern shape and steering velocity.

Note that SL_d differs from the loss on the raw data signal, i.e., the PEL in (9). To clarify this statement, let us consider the PEL for a homogeneous imaged scene (Appendix B):

$$PEL(t_0) = \frac{\sum_{t=t_0-T/2}^{t_0+T/2} \left| AF_n(\theta_{\text{exp}}(t_0), \theta_{\text{act}}(t)) \right|^2}{N_s}. \quad (27)$$

Here, the SCORE pattern is steered towards the expected direction of arrival at the instant t_0 , $\theta_{\text{exp}}(t_0)$, and computed over the footprint on ground of the pulse, i.e., $\theta_{\text{act}}(t)$ for $|t - t_0| \leq T/2$ [12]. In contrast to this, for the SL_d in (25), the pattern is computed only in $\theta_{\text{act}}(t_0)$ according to the steering variation within the pulse duration. Moreover, for the considered planar array, $AF(\theta_1, \theta_2) = AF(\theta_2, \theta_1)$ and (27) can be equivalently written as

$$PEL(t_0) = \frac{\sum_{t=t_0-T/2}^{t_0+T/2} \left| AF_n(\theta_{\text{act}}(t), \theta_{\text{exp}}(t_0)) \right|^2}{N_s}. \quad (28)$$

Accordingly, $PEL(t_0) = SL_d(t_0)$ only if $\theta_{\text{exp}}(t) = \theta_{\text{act}}(t)$. However, since $\theta_{\text{exp}}(t)$ is constant vs. azimuth time, the previous condition could be eventually satisfied for a specific range line, but not for the whole SAR image, unless the imaged scene has no topographic variations in the azimuth direction. Indeed, as shown by the numerical analysis in Section VII.C, the two losses could be significantly different, depending on the system and acquisition parameters.

VI. SCORE LOSS AND SAR RX WINDOW

In the SAR processing, a Rx window,

$$w_{Rx}(t), \quad |t| \leq T/2, \quad (29)$$

such as a Hamming window, can be used at range compression stage (instead of the rectangular window, considered till now), in order to reduce the IRF sidelobe level [25]. In this case, the transfer function in (17) must be generalized by including the Rx window at range compression level. Accordingly, the SL expressions become:

$$SL_p(t_0) = \frac{\left| \sum_{t=t_0-T/2}^{t_0+T/2} w_{Rx}(t-t_0) AF_n(\theta_{\text{exp}}(t), \theta_{\text{act}}(t_0)) \right|^2}{\left| \sum_{t=-T/2}^{T/2} w_{Rx}(t) \right|^2}, \quad (30)$$

$$\begin{aligned} SL_d(t_0) &= \frac{\sum_{t=t_0-T/2}^{t_0+T/2} \left| w_{Rx}(t-t_0) AF_n(\theta_{\text{exp}}(t), \theta_{\text{act}}(t_0)) \right|^2}{\sum_{t=-T/2}^{T/2} |w_{Rx}(t)|^2} = \\ &= SL_e(t_0). \end{aligned} \quad (31)$$

VII. NUMERICAL ANALYSIS

A. Simulation Frame

The effect of unmodelled terrain height and pulse duration on the SCORE image formation process is investigated numerically by means of an end-to-end (E2E) simulator. The simulation procedure reflects the data model in Section II and the block diagram in Fig. 2. As a benchmark, the conventional SAR image formation (Fig. 3), based on a single Rx channel, is simulated too.

Unless explicitly stated otherwise, the reference scenario in Table I is considered: an X-band SAR system, orbiting at an altitude of 514 km; the planar array antenna is 1 m high and composed of 25 digital channels; the pulse duration is 56 μ s.

The expected DoA, i.e., the SCORE steering law, is based on a pure spherical Earth model with no terrain height ($h = 0$ m), as in the original SCORE formulation [1], [2]. The actual DoA, used to simulate the reflectivity, is based on the topographic profile in Fig. 7: the unmodelled terrain height, Δh , is 0 m in near range, increases linearly until 2000 m, and remains constant in far range.

As regards the SAR processing, a rectangular Rx window is assumed at the range compression stage, if not otherwise specified.

Concerning the imaged surface, both a single point target and a distributed target are simulated. Specifically, three kinds of ground reflectivity functions are considered:

TABLE I
REFERENCE SYSTEM PARAMETERS

Quantity	Value
Orbit Height, H_{orb}	514 km
Antenna Tilt Angle (w.r.t. Nadir), θ_{tilt}	29.18 deg
Rx Antenna Height, h_{ant}	1 m
Nr. of Digital Rx Elev. Channels, K	25
RF Center Frequency	9.65 GHz
Chirp Duration, T	56 μ s
Chirp Bandwidth, B_c	100 MHz
Range Sampling Frequency, S_f	109.88 MHz

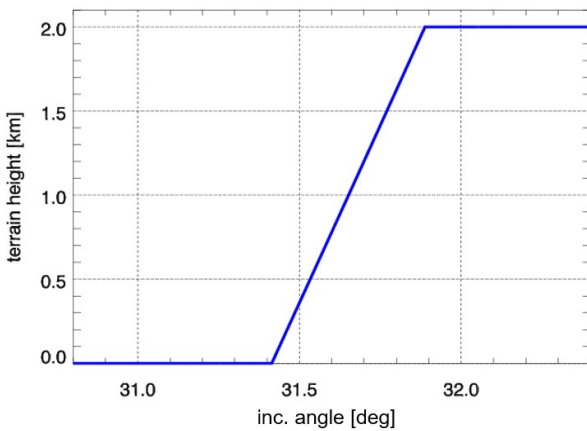


Fig. 7. Reference scenario: actual topographic profile in the zero-Doppler plane vs. incidence angle.

- (i) a Dirac delta (for the point targets in Table II);
- (ii) a stationary, WCG process with zero mean and mean power σ^2 (Fig. 8);

(iii) a range line extracted from a real TerraSAR-X (TSX) [18], slant-range, single-look, complex (SSC) SAR image, illustrating the Amazonas forest or a rural area (Fig. 8); where the simulated WCG process has a mean power given by the mean intensity of the Amazonas TSX image.

The SL for a point target is computed numerically, based on a single (interpolated) range line of the simulated SAR images, $q(t)$ and $q_c(t)$, as

$$SL_p(t_0) = \frac{|q(t_0)|^2}{K^2 |q_c(t_0)|^2}, \quad (32)$$

$$SL_e(t_0) = \frac{\sum_i |q(t_i)|^2}{K^2 \sum_i |q_c(t_i)|^2}. \quad (33)$$

For a distributed target, 1000 statistically identically distributed range lines of the output SAR images are generated and combined as

$$SL_d(t_0) = \frac{\sum_{n=1}^{1000} |q(t_0, n)|^2}{K^2 \sum_{n=1}^{1000} |q_c(t_0, n)|^2} \approx \frac{E\{|q(t_0)|^2\}}{K^2 E\{|q_c(t_0)|^2\}}. \quad (34)$$

The SL on the raw data, i.e., the PEL [12], is computed as:

$$PEL(t_0) = \frac{\sum_{n=1}^{1000} |s(t_0, n)|^2}{K^2 \sum_{n=1}^{1000} |r_k(t_0, n)|^2} \approx \frac{E\{|s(t_0)|^2\}}{K^2 E\{|r(t_0)|^2\}}. \quad (35)$$

Note that the inputs/outputs of the E2E simulator are generated vs. range time. Nevertheless, in order to provide a clearer information on the geometry, they are illustrated in the reported figures vs. incidence angle (angle corresponding to the range time, based on a pure spherical model).

TABLE II
SINGLE POINT TARGET SCENARIOS

Quantity	Value#1	Value#2
Unmodelled Terrain Height, Δh	0 m	1999 m
Incidence Angle	30.9999 deg	31.8883 deg
Expected DoA, θ_{exp}	28.4653 deg	29.2662 deg
Actual DoA, θ_{act}	28.4653 deg	29.6277 deg

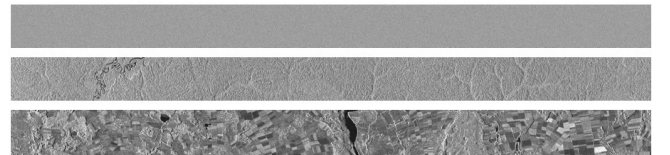


Fig. 8. Matrix of 1000 range lines representing the amplitude of: the simulated WCG process (top); a cut of an SSC TSX image [18] representing the Amazonas (center), and a rural area around Munich (bottom). Each complex range line is used as input ground reflectivity of the E2E simulator.

B. Point Target Analysis

Let us first refer to the two point targets in Table II, to investigate the effect of unmodelled topography and pulse duration on the SCORE IRF.

Figs. 9.a and 10.a show the normalized SCORE pattern values, $AF_n(\theta_{act}(t_0), \theta_{exp}(t))$, $|t - t_0| \leq T/2$, weighting the Rx chirp echo according to (16). As comparison, a typical Hamming Rx window (with coefficient $\alpha = 0.6$) is reported too. The figures describe the mutual effect of T and Δh on the SCORE pattern sector, weighting the Rx samples. In particular, T determines the angular extension of the pattern sector, according to the SCORE steering velocity at the target position (see Fig. 4); Δh determines the value around which the pattern sector is centered, $AF_n(\theta_{exp}(t_0), \theta_{act}(t_0))$. Note that this pattern value defines the SL for a very short pulse in (24), and $\theta_{act}(t_0) - \theta_{exp}(t_0)$ represents the topographic steering error (in Fig. 5). The obtained topographic steering error is equal to 0 deg and 0.36 deg, respectively, for the target in near and far range. The angular extension of the pattern sectors is around 1.3 deg for both targets. In near range, where no topographic mismatch is present, the sector is almost symmetric, and all the values are within the HPBW. In far range, due to the unexpected topography, the sector shifts and becomes visibly asymmetric. Here pattern values outside the HPBW also weight the Rx signal. The interval of pattern values is anyway less extended than that of the Hamming window.

Figs. 9.b-c and 10.b-c show the IRF vs. incidence angle; the ideal IRF (with SL = 1) is reported too, as benchmark. All the figures, except Fig. 10.c, assume a rectangular Rx window at the range compression stage. Fig. 10.c shows the IRF for a Hamming Rx window with coefficient $\alpha = 0.6$. The plots show that energy, maximum value, and sidelobe level of the SCORE IRF are lower than the corresponding ideal values; however, almost no variation of the main lobe width (range resolution) is present. In particular, when the rectangular Rx window is considered, the loss on the IRF peak power and energy are around -0.67 dB in near range, and -1.1 dB in far range. The peak-to-sidelobe ratio improves by about 1.5 dB.

As shown by the zoom in Fig. 9.c, the measured peak power degradation corresponds with the expected theoretical value of SL_p (in the title of the figure); the measured energy degradation reflects the expected SL_e value too (the difference between measured and expected value is well below 10^{-3}).

The obtained results indicate that the radiometric degradation could be significant, especially considering the demanding requirements on the quality of future SAR images (the radiometric stability and accuracy must be in the order of 0.5 dB). The other effects seem not critical. Indeed, the sidelobe reduction is a positive effect, and could be eventually considered to optimize the choice of the Rx window.

Figs. 9 and 10 evidence that, if the SCORE pattern sector is asymmetric, the IRF is not real (as in the ideal case) but has an antisymmetric imaginary component. The SAR Rx window plays also a role (Fig. 10.c). Accordingly, the phase of the IRF depends on the target position, the SCORE pattern, the assumed steering law, and the Rx window.

Fig. 11 shows the phase difference between the IRFs of two identical SCORE SAR systems, whose antenna arrays are separated by a cross-track interferometric baseline. In particular, the figure is obtained for the target in far range, based on the reference scenario, assuming that the two arrays, each with $K = 25$ elements and a height of 1 m, are located on the same platform, as lower and upper portion of a 2 m high array with $K = 50$ elements. As a comparison, the phase difference between conventional IRFs, obtained from the central channels of each array are reported. As expected, the phase difference between SCORE IRFs is constant and given by the interferometric phase associated with the target position, as in the conventional case. Actually, the SCORE interferometric phase is more stable compared to the conventional one, due to the average performed by the DBF.

Based on the results in Figs. 9-11, it is possible to conclude that the phase of a SCORE SAR image representing a distributed target will differ in general in a noisy way from the conventional one. However, the interferometric phase extracted from SCORE images is not affected by topographic variations and pulse duration, as long as the actual DoA and the SCORE pattern are the same for the combined images. It is worth to remark that a deviation from this condition may occur, due for instance to attitude and calibration errors. The analysis of this effect goes anyway beyond the aim of the present work. The next section focuses on the SAR image radiometric degradation associated with topographic variations and pulse duration.

C. Distributed Target Analysis

Let us now consider a distributed target. As shown in Sections V and VI, the SL depends on the terrain height, the pulse duration, the SCORE pattern shape and steering law, the location (in near or far range) of the imaged area, and the SAR Rx window. In order to evaluate the individual influence of these quantities, the following numerical analysis starts from the reference scenario (Table I, Fig. 7, rectangular Rx window) and moves then to scenarios obtained from the reference one by varying a single parameter of interest.

Fig. 12 illustrates the SL on the simulated SCORE SAR image vs. incidence angle for the reference scenario. The considered input reflectivities are the realizations of the WCG process, and the range lines of the TSX image of the Amazonas (Fig. 8). Together with the obtained numerical values, the expected theoretical ones, in (22) and (25), for point and distributed targets, are indicated. Additionally, the SL for a very short pulse in (24) is reported as benchmark. It represents the loss introduced exclusively by the topography, whereas the other curves show the mutual effect of topography and pulse duration. In particular, in near range, where $\Delta h = 0$, only the pulse duration is responsible for the SL, whereas, in far range, both effects are present.

The SL obtained from the WCG process matches the expected theoretical value, and varies between about -0.66 dB and -1.1 dB from near to far range. The SL obtained from the TSX image of the Amazonas improves by about 0.4 dB, in comparison. This mismatch evidences the effect of a possible correlation between reflectivity samples (resolution cells). In fact, the TSX processor introduces a correlation on the

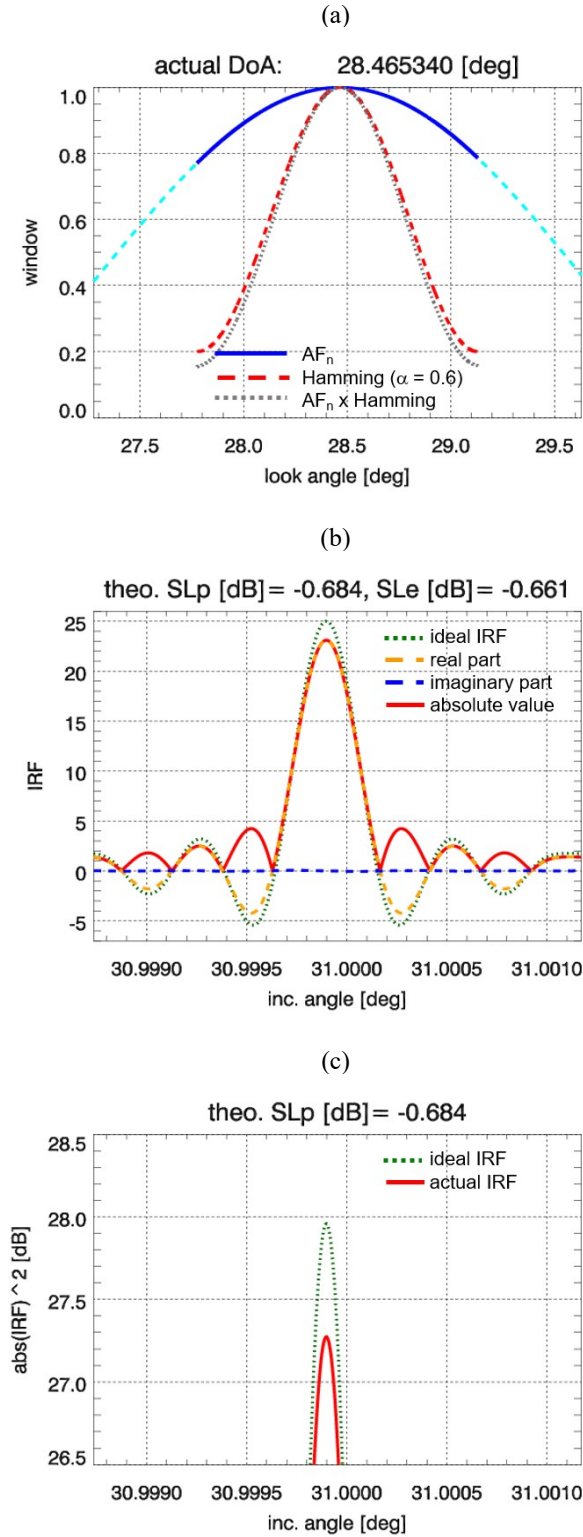


Fig. 9 Reference scenario (Table I, Fig. 7). Point target in near range (Table II, $\Delta h = 0$ m). Top: normalized SCORE pattern window (i.e., values of the normalized SCORE pattern, AF_n , weighting the Rx samples); Hamming Rx window ($\alpha = 0.6$) as comparison. Center: simulated IRF of the SCORE system (with rectangular Rx window). Bottom: zoom of the IRF intensity in dB.

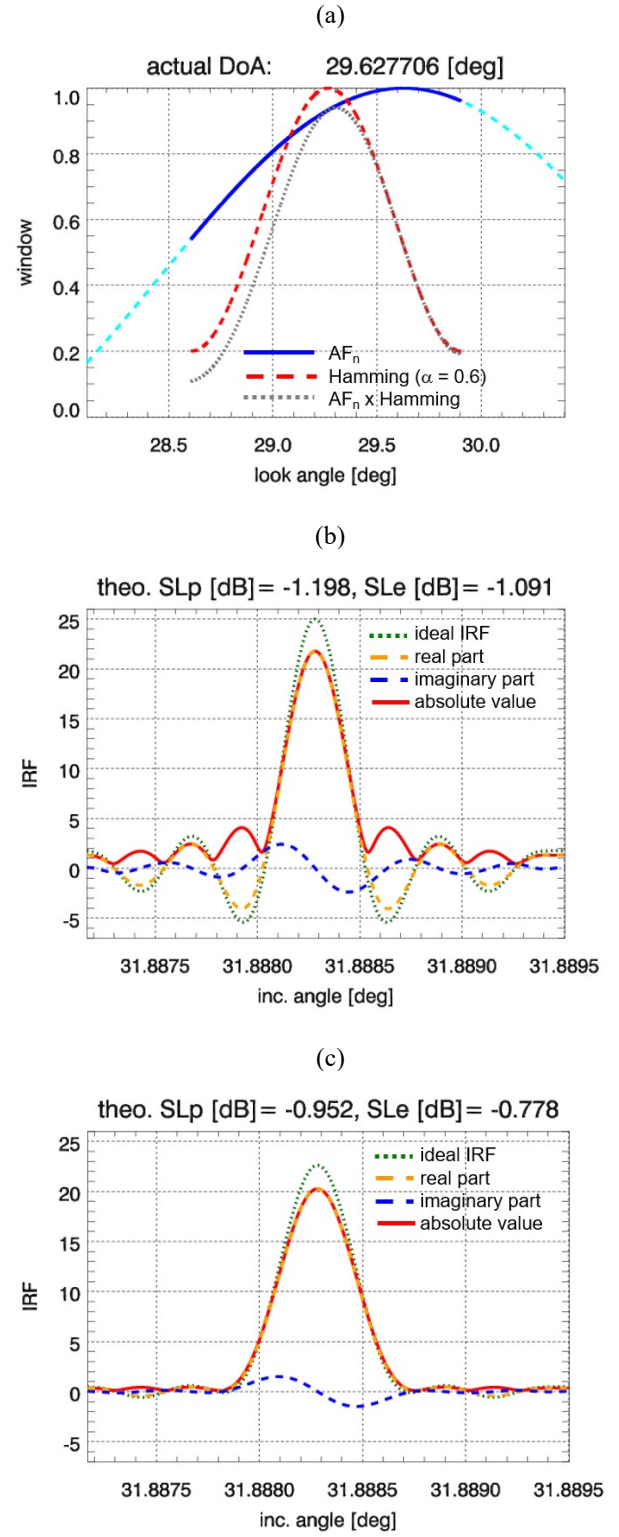


Fig. 10. Reference scenario (Table I, Fig. 7). Point target in far range (Table II, $\Delta h = 1999$ m). Top: normalized SCORE pattern window (i.e., values of the normalized SCORE pattern, AF_n , weighting the Rx samples); Hamming Rx window ($\alpha = 0.6$) as comparison. Center: simulated IRF of the SCORE system (with rectangular Rx window). Bottom: simulated IRF of the SCORE system, with Hamming Rx window ($\alpha = 0.6$).

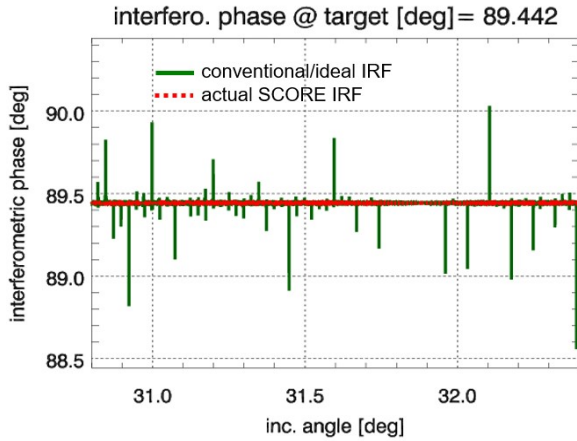


Fig. 11. Reference scenario (Table I, Fig. 7). Point target in far range (Table II, $\Delta h = 1999$ m). Phase difference between SCORE IRFs (obtained by two arrays, as the reference one, separated by an interferometric baseline of 1 m), and phase difference between conventional/ideal IRFs (obtained from the central channel of each array). The expected interferometric phase associated with the target position is reported in the title.

Amazonas image. As a consequence, even if in both cases the samples of the input reflectivity functions are $CG(0, \sigma^2)$, they are independent only for the WCG process.

Fig. 13 highlights the effect of the pulse duration, which is here halved to $28 \mu s$ compared to the reference value. As expected, the SL improves when the pulse duration reduces. For $T = 28 \mu s$ the SL decreases by about 0.4 dB compared to the SL in Fig. 12. However, even in this case the loss is not negligible. In the limiting case of a very short pulse (black dotted curve) the SL would further improve by about 0.2 dB. It is anyway worth to remark that the pulse duration cannot be arbitrarily short, due to the antenna thermal and power constraints.

Fig. 14 highlights the effect of the swath location, which is here shifted in far range. The SL improves by about 0.3 - 0.6 dB compared to the SL in Fig. 12, due to the lower SCORE steering velocity (see Fig. 4). The dependence of the SL on the range position cannot be neglected.

Fig. 15 is obtained by considering the Rx window of the TSX processor: a Hamming window with $\alpha = 0.6$. The comparison with Fig. 12 evidences the strong dependence of the SL on the choice of the Rx window. Moreover, it shows that the SL obtained from the TSX image of the Amazonas (with a rectangular Rx window) is similar to that obtained from the WCG reflectivity with the TSX window on Rx. This suggests that the correlation between pixels of the Amazonas image is due mainly to the Hamming Rx window of the TSX processor, which shapes the PSD of the Amazonas reflectivity.

Fig. 16 investigates the influence of the SCORE steering law. It is obtained by assuming a SCORE steering law that perfectly matches the actual topographic profile (Fig. 7). The correspondence between the obtained SL and the expected one confirms the validity of the derived expressions for a general steering. The comparison with Fig. 12 highlights the strong dependence of the SL on the assumed steering law. The maximum loss is reached at the swath center, where the topographic profile increases linearly with the slant range (see Fig. 7). In fact, here the SCORE pattern sector weighting the

signal received from a resolution cell has the maximum width, i.e., the SCORE steering velocity assumes the highest values during the pulse echo duration. It is worth to note that, for an actual topography with negative slope, the minimum loss occurs at the swath center. This suggests the possibility to use the derived SL expression to optimize the SCORE steering law according to the actual topography.

Fig. 16 also shows that, even if the topographic error is zero (see the SL for a very short pulse), the SL depends on the actual topography and the assumed steering law through the pulse duration. It must be emphasized that the compensation of the pulse extension by a frequency-dispersive SCORE could be extremely complicated, eventually not realistic, for acquisition scenarios characterized by fast topographic variations. This highlights the importance to consider the mutual effect of pulse duration, topographic variation, and steering law.

The results in Figs. 12-16 indicate that the radiometric loss, associated with topographic variations and pulse duration, can reach values larger than 1 dB, depending on the system parameters and acquisition geometry. This is true for point and distributed targets. Indeed, the loss on the IRF peak power is even larger than the SL for a distributed target, with a difference that depends on the system and acquisition parameters. Such a loss cannot be neglected, if the radiometric accuracy and stability of future SAR images must be in the order of 0.5 dB. In particular, the effect must be considered not only to properly predict the achievable SAR imaging performance of the SCORE system, but also to retrieve the SAR signal intensity by means of the external calibration. The derived SL expressions, for distributed and point targets, appear then as a novel important support for both of these tasks.

As mentioned in the previous sections, the effect of pulse duration and topographic variations on SCORE is described so far in the literature by the PEL, as a loss on the Rx power [12]. In order to clarify the difference between the proposed SL_d and the PEL, Fig. 17 reports the loss on the simulated SAR raw data (after DBF) and the expected PEL, for the reference scenario. They are computed according to (35) and (27), respectively. The comparison with Fig. 12 shows that the difference between SL_d and PEL could be important. In fact, the two curves have a completely different trend vs. slant range. Moreover, the worst value of the PEL is about 0.23 dB larger than the SL. This confirms the unadequacy of the PEL to describe the SCORE SAR imaging performance.

The results reported so far refer to distributed uniform targets. A less homogeneous surface, the rural area in Fig. 8, is considered in Fig. 18. The simulation parameters are those of the reference scenario, except for the actual topographic profile, which was changed in order to make the SL clearly visible on the simulated SAR image (see Fig. 18, top and center). The theoretical SL is here computed according to (26) as

$$SL_d(t_0) = \frac{\sum_{t=t_0-T/2}^{t_0+T/2} |w_H(t-t_0) AF_n(\theta_{exp}(t), \theta_{act}(t_0))|^2}{\sum_{t=-T/2}^{T/2} |w_H(t)|^2}, \quad (36)$$

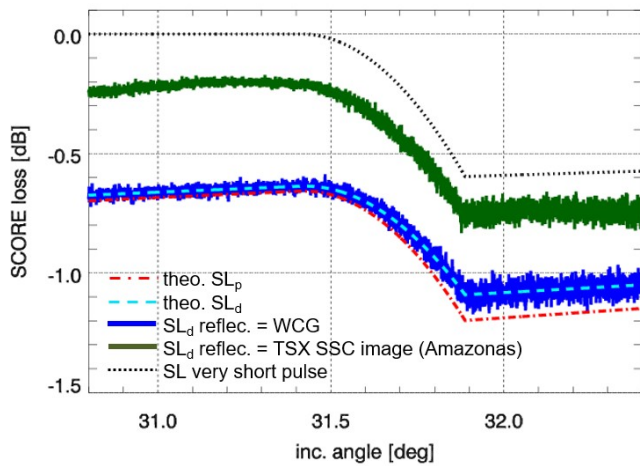


Fig. 12. Distributed target: SL vs. incidence angle. Reference scenario (Table I, Fig. 7, rectangular Rx window).

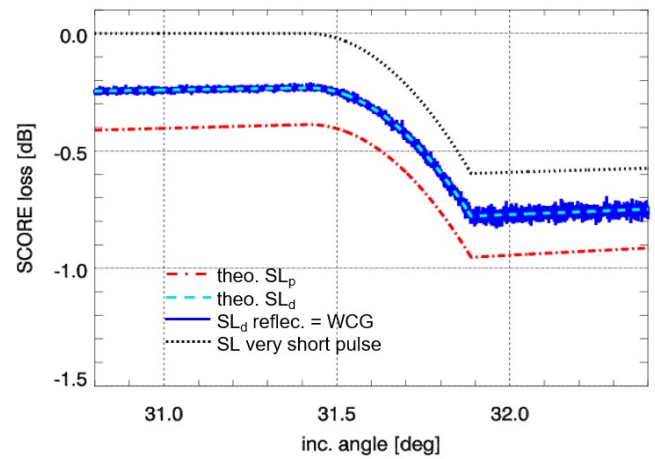


Fig. 15. Distributed target: SL vs. incidence angle. Reference scenario, except for the Rx window at the range compression stage: here a Hamming window ($\alpha = 0.6$) is assumed, the same used by the TSX processor.

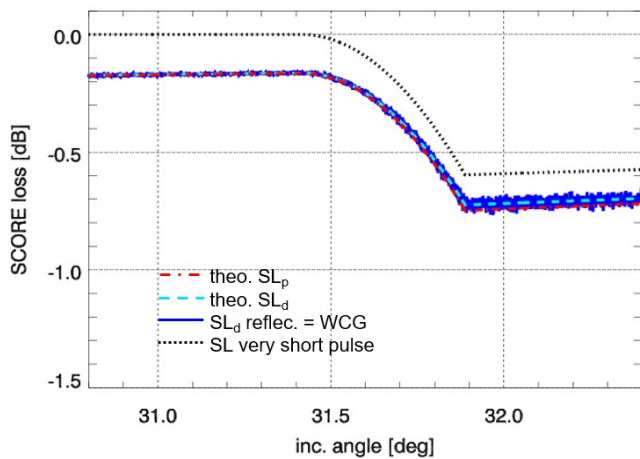


Fig. 13. Distributed target: SL vs. incidence angle. Reference scenario, except for the pulse duration: here $T = 28 \mu s$.

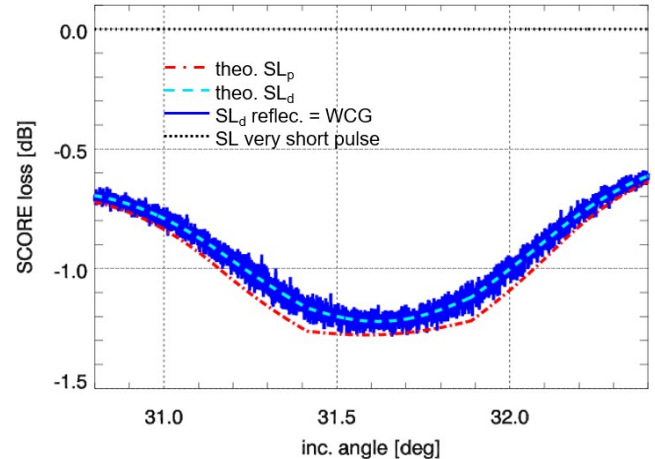


Fig. 16. Distributed target: SL vs. incidence angle. Reference scenario, except for the steering law: here the expected DoA perfectly matches the actual DoA in Fig. 7.

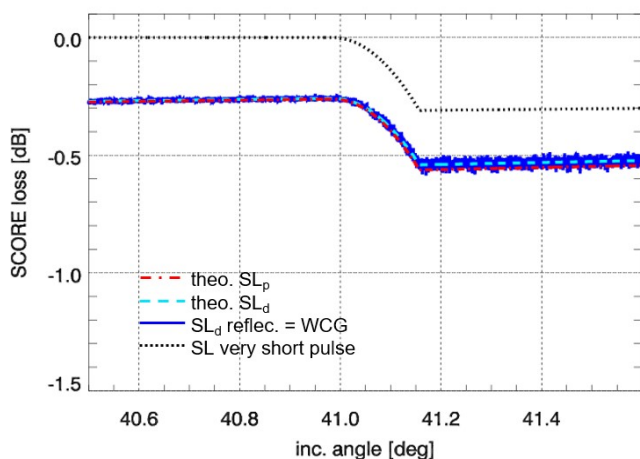


Fig. 14. Distributed target: SL vs. incidence angle. Reference scenario, except for the swath location: here the swath is moved in far range.

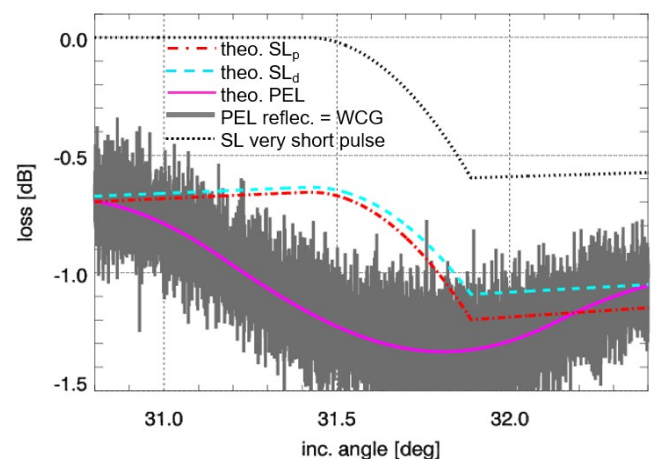


Fig. 17. Distributed target: SL and PEL vs. incidence angle. Reference scenario.

where w_H is the Hamming window ($\alpha = 0.6$) used by the TSX processor at the range compression stage, assumed to be a scaled version of the input ground reflectivity PSD. The numerical value of the SL is obtained according to (34), by averaging, in the azimuth direction, 1000 samples of the simulated range lines. It is worth to remark that (34) relies on the assumption that the range lines are homogeneous (identically distributed) in the azimuth direction, which is true only approximately (see the dashed circles in the top of the figure). As shown in Fig. 18, the obtained numerical value of the SL confirms the theoretical prediction, even showing some residual fluctuation in correspondence of the mentioned heterogeneities.

Finally, it is worth to remark that, for a distributed target, each single range line of the SCORE SAR image is not an exact scaled version of the corresponding ideal one. This is due to the time-varying nature of the image formation process, described by (17). In fact, SL_d represents the ratio between the mean power of corresponding pixels, in the actual SCORE SAR image and the ideal one. This is shown in Fig. 19, for the previous rural area scenario, where the ratio between the intensity of two corresponding range lines is reported together with the theoretical SL_d . Nevertheless, the relationship between the SCORE SAR image and the ideal one is deterministic, and given by the derived equivalent LTV filter in (17). In particular, for a point target, the values of peak power and energy are scaled by SL_p and SL_e , respectively, compared to the ideal values. It is then reasonable to assume that the knowledge on the equivalent LTV filter could be exploited in order to compensate the losses on the SCORE SAR image.

VIII. CONCLUSION

The mutual effect of topographic variations and pulse duration on the SAR imaging performance of future spaceborne systems with scan-on-receive (SCORE) capability is investigated, both from an analytical and numerical perspective. The basic SCORE formulation for short pulses is considered, as first relevant case of interest.

A novel description of the SAR image formation process, as a linear time-varying (LTV) filter, is presented. The related IRF is derived and analyzed, showing that the main effect of unmodelled terrain height and pulse duration is a reduction of the peak power and energy of the IRF. A new mathematical expression of the radiometric degradation, denoted as the SCORE loss (SL), is demonstrated. This makes it possible to predict and quantify the radiometric loss at SAR image level, based on the knowledge of system, processing, and geometric parameters. The contribution of the SAR processing Rx window is also included and described for the first time.

The effect of the topographic variations and pulse duration is further investigated numerically, by means of an end-to-end simulator, in different acquisition scenarios. The obtained results indicate that, due to unmodelled topographic variations and pulse duration, a significant degradation of the SAR image radiometric quality may occur. In fact, the amount of degradation can reach values higher than 1 dB, and depends

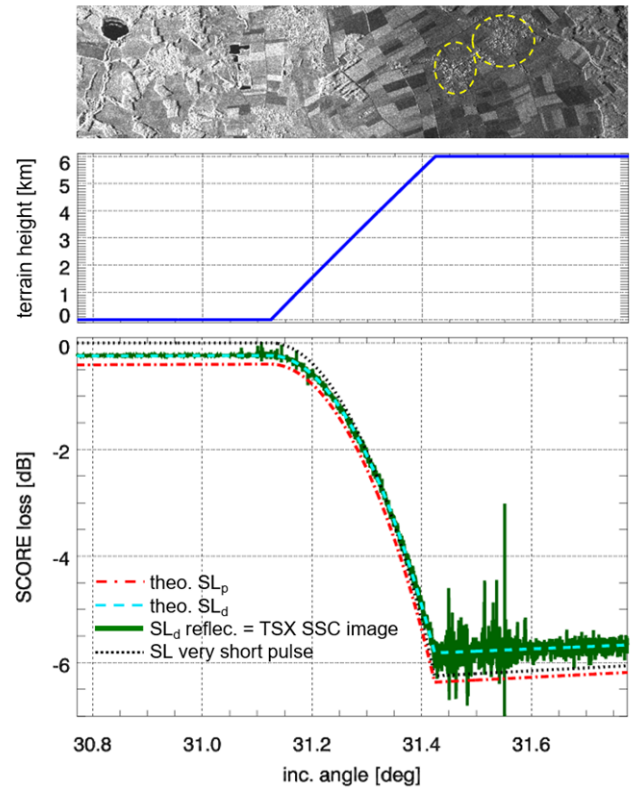


Fig. 18. Rural area scenario: simulated SCORE SAR image (top); actual topographic profile (center); SL (bottom).

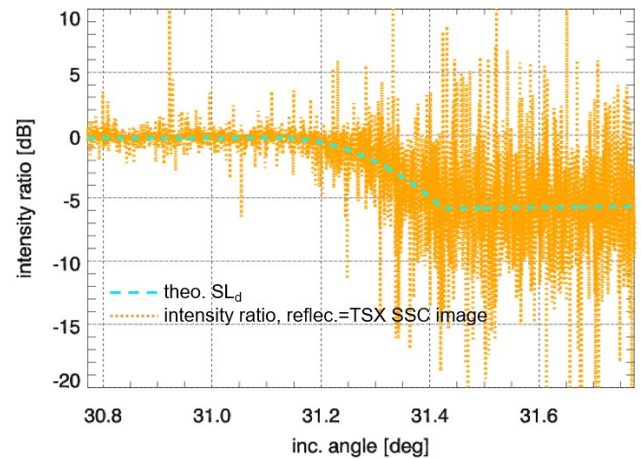


Fig. 19. Rural area scenario: ratio between the intensity of a range line of the simulated SCORE SAR image and the corresponding ideal one. The theoretical value of the SL for a distributed target is reported as comparison.

on the SCORE pattern shape and steering law, the slant range position, the statistical properties of the backscattering, the SAR processing Rx window. Such a loss and its dependence on the acquisition parameters cannot be neglected, if the radiometric accuracy and stability of future SAR images must be in the order of 0.5 dB.

The derived expression of the IRF and of the SL appear then as a novel useful tool for DBF SAR, able to support tasks of system design, imaging performance prediction, and external calibration. A further possible application is the

optimization of the SCORE steering law, based on the acquisition scenario. Moreover, it is reasonable to assume that the knowledge on the derived equivalent LTV filter could be used in order to compensate the effect of topographic variations and pulse duration on the SAR image.

APPENDIX A: LOSS ON THE SAR IMAGE

Let us consider a homogeneous imaged scene. The ground reflectivity, $g(t)$, can be modelled as a stationary WCG process with zero mean, and mean power [21]

$$\sigma^2 = E\{|g(t)|^2\} = \int S_g(f) df, \quad (37)$$

where $S_g(f)$ denotes the PSD, constant w.r.t. frequency at least over the chirp bandwidth.

The SL in (10) can be then derived based on the transfer function of the filters in (17)-(19) as [24]

$$\begin{aligned} SL_d(t_0) &= \frac{E\{|q(t_0)|^2\}}{K^2 E\{|q_c(t_0)|^2\}} = \frac{\int S_g(f) |H_s(f, t_0)|^2 df}{K^2 \int S_g(f) |C(f)|^4 df} = \\ &= \frac{\int |H_s(f, t_0)|^2 df}{K^2 \int |C(f)|^4 df} = SL_e(t_0) = \\ &= \frac{\sum_{t=t_0-T/2}^{t_0+T/2} |AF_n(\theta_{\exp}(t), \theta_{act}(t_0))|^2}{N_s}, \end{aligned} \quad (38)$$

where AF_n denotes the normalized SCORE pattern array factor, steered towards $\theta_{\exp}(t)$ and computed in $\theta_{act}(t_0)$. Accordingly, the SL for a given pixel of the SAR image is determined by the SCORE pattern values weighting the signal received from the corresponding imaged area (resolution cell). Indeed, (38) still applies even if the condition of homogeneity is not satisfied, as long as the ground reflectivity samples can be modelled as independent, random, variables with zero mean.

APPENDIX B: LOSS ON THE RAW DATA

Let us consider a homogeneous imaged scene. The signal received at the instant t_0 by means of the SCORE pattern is

$$s(t_0) = \sum_{t=-T/2+t_0}^{+T/2+t_0} g(t) c(t_0-t) AF(\theta_{\exp}(t_0), \theta_{act}(t)), \quad (39)$$

where $|c(t)| = 1$, and $g(t)$ is the ground reflectivity, modelled as a WCG process, whose samples are independent CG random variables, with zero mean and variance σ^2 , i.e., $g(t) \in CG(0, \sigma^2)$; AF is the SCORE pattern, which is steered towards $\theta_{\exp}(t_0)$ and computed over the instantaneous footprint on ground of the pulse, i.e., $\theta_{act}(t)$ for $|t - t_0| \leq T/2$ [12].

The mean power of the Rx signal, at the instant t_0 , is given by the variance of $s(t_0)$:

$$E\{|s(t_0)|^2\} = \sigma^2 \sum_{t=-T/2+t_0}^{+T/2+t_0} |AF(\theta_{\exp}(t_0), \theta_{act}(t))|^2, \quad (40)$$

where the equation relies on the independence of the ground reflectivity samples and their identical distribution. In the ideal case of no losses,

$$E\{|s(t_0)|^2\} = \sigma^2 N_s K^2. \quad (41)$$

Accordingly, the loss on the raw data signal (after DBF) is given by

$$SL_r(t_0) = \frac{\sum_{t=-T/2+t_0}^{+T/2+t_0} |AF_n(\theta_{\exp}(t_0), \theta_{act}(t))|^2}{N_s} = PEL(t_0). \quad (42)$$

This expression is known in the literature as pulse extension loss (PEL) [12].

ACKNOWLEDGMENT

The authors thank Prof. A. Jakobsson, Lund University, Lund, Sweden, and the Department of Mathematical Statistics of the Lund University for having made possible and supported D. Lind's master's thesis internship at the Microwaves and Radar Institute of the German Aerospace Centre.

REFERENCES

- [1] M. Suess, B. Grafmueller, R. Zahn, "A Novel High Resolution, Wide Swath SAR System", in *Proc. IEEE IGARSS*, Sydney, NSW, Australia, 2001, pp. 1013-1015.
- [2] M. Suess and W. Wiesbeck, "Side-Looking Synthetic Aperture Radar System", European Patent Application, EP 1 241 487 A1, Sept. 18, 2002.
- [3] G. Krieger, N. Gebert, A. Moreira, "Unambiguous SAR signal reconstruction from nonuniform displaced phase center sampling", *IEEE Trans. Geosci. and Remote Sens. Letters*, vol. 1, no. 4, pp. 260 - 264, Oct. 2004.
- [4] G. Krieger, N. Gebert, A. Moreira, "Multidimensional Waveform Encoding: A New Digital Beamforming Technique for Synthetic Aperture Radar Remote Sensing", *IEEE Trans. on Geosci. and Remote Sens.*, vol. 46, no. 1, pp.31-46, Jan. 2008
- [5] N. Gebert, G. Krieger, and A. Moreira, "Digital Beamforming on Receive: Techniques and Optimization Strategies for High-Resolution Wide-Swath SAR Imaging", *IEEE Trans. on Aero. and Electron. Sys.*, vol. 45, no. 2, pp. 564-592, April 2009.
- [6] F. Feng, S. Li, W. Yu, P. Huang, W. Xu, "Echo Separation in Multidimensional Waveform Encoding SAR Remote Sensing Using an Advanced Null-Steering Beamformer", *IEEE Trans. on Geosci. and Remote Sens.*, vol. 50, no. 10, pp.4157-4172, Oct. 2012.
- [7] P. Rosen, R. Kumar, "NASA-ISRO SAR (NISAR) Mission Status", in *Proc. IEEE RadarConf*, Atlanta, GA, USA, 2021, pp. 1-6.
- [8] S. Miura, Y. Kankaku, T. Motohka, K. Yamamoto, S. Suzuki, "ALOS-4 Current Status", in *Proc. SPIE Sensors, Systems, and Next-Generation Satellites XXV*, vol. 11858 1185809, SPIE Remote Sens., Online Only, Sept. 2021, pp. 1-10.
- [9] D. Geudtner, N. Gebert, M. Tossaint, M. Davidson, F. Heliere, I. Navas Traver, R. Furnell, R. Torres, "Copernicus and ESA SAR Missions", in *Proc. IEEE RadarConf*, Atlanta, GA, USA, 2021, pp. 1-6.
- [10] A. Moreira, G. Krieger, I. Hajnsek, K. Papathanassiou, M. Younis, P. Lopez-Dekker, S. Huber, M. Villano, M. Pardini, "Tandem-L: A Highly Innovative Bistatic SAR Mission for Global Observation of Dynamic Processes on the Earth's Surface", *IEEE Geosci. and Remote Sens. Magazine*, vol. 3, no. 2, pp. 8-23, June 2015.

- [11] A. Moreira *et al.*, “Tandem-L: Project Status and Main Findings of the Phase B1 Study”, in *Proc. IEEE IGARSS*, Valencia, Spain, 2018, pp. 8667-8670.
- [12] M. Younis, T. Rommel, F. Bordonì, G. Krieger, A. Moreira, “On the Pulse Extension Loss in Digital Beamforming SAR”, *IEEE Geosci. and Remote Sens. Letters*, vol. 12, No. 7, pp. 1436 – 1440, Oct. 2015.
- [13] F. Bordonì, M. Rodriguez, P. Prats, G. Krieger, “The Effect of Topography on SCORE: an Investigation Based on Simulated Spaceborne Multichannel SAR Data”, in *Proc. EUSAR*, Aachen, DE, 2018, pp.1130-1134.
- [14] F. Bordonì, M. Rodriguez, G. Krieger, “Possible Sources of Imaging Performance Degradation in Advanced Spaceborne SAR Systems Based on Scan-On-Receive”, in *Proc. IEEE RadarConf*, Florence, IT, 2020, pp. 1-4.
- [15] F. Feng, H. Dang, X. Tan, G. Li, C. Li, “An improved scheme of Digital Beam-Forming in elevation for spaceborne SAR”, in *Proc. IET Inter. Radar Conf.*, Xi'an, China, April 2013, pp. 1-4.
- [16] S. Huber, M. Younis, G. Krieger, A. Patyuchenko, A. Moreira, “Spaceborne Reflector SAR Systems with Digital Beamforming”, *IEEE Trans. on Aerospace and Electronic Systems*, vol. 48, no. 4, pp. 3473-3493, Oct. 2012.
- [17] Q. Zhao, Y. Zhang, W. Wang, K. Liu, Y. Deng, H. Zhang, Y. Wang, Y. Zhou, R. Wang, “On the Frequency Dispersion in DBF SAR and Digital Scaloped Beamforming”, *IEEE Trans. on Geosci. and Remote Sens.*, vol. 58, no. 5, pp. 3619-3632, May 2020.
- [18] G. Krieger, A. Moreira, H. Fiedler, I. Hajnsek, M. Werner, M. Younis, M. Zink, “TanDEM-X: A Satellite Formation for High Resolution SAR Interferometry”, *IEEE Trans. on Geosci. and Remote Sens.*, vol. 45 (11), pp. 3317-3341, 2007.
- [19] F. Bordonì, D. Lind, A. Jakobsson, G. Krieger, “Unconventional Sources of Error in High-Resolution Wide-Swath SAR Systems based on Scan-On-Receive”, in *Proc. EUSAR*, Leipzig, DE, 2021, pp. 1116-1119.
- [20] D. Lind, “Future Spaceborne SAR Systems based on SCORE: Intrinsic Limitations and Possible Solutions”, Master Thesis, Lund University, Sweden, April 2021.
- [21] J. C. Curlander, R. N. McDonough, *Synthetic Aperture Radar: Systems and Signal Processing*. New York, USA: Wiley, 1991.
- [22] Z. Chen, Z. Zhang, J. Qiu, Q. Zhao, H. Fan, “A Novel Aperture Extension Loss Compensation Scheme and Azimuth Ambiguity Suppression Method for Airborne Elevation DBF-SAR”, *IEEE Trans. on Geosci. and Remote Sen.*, pp. 1-11, August, 27, 2021, DOI: 10.1109/TGRS.2021.3103113, [Online Early Access].
- [23] A. Freeman, C. Curlander, “Radiometric Correction and Calibration of SAR Images”, *Photogrammetric Engineering & Remote Sensing*, vol. 55, no. 9, pp. 1295-1301, Sep. 1989.
- [24] P. Stoica, R. Moses, *Introduction to Spectral Analysis*. Upper Saddle River, NJ, USA: Prentice Hall, 1997.
- [25] I. G. Cumming, F. H. Wong, *Digital Processing of Synthetic Aperture Radar Data, Algorithms and Implementation*, Boston, USA: Artech House, 2005.



Federica Bordonì received the Laurea (M.S.) degree in telecommunication engineering and the Ph.D. degree in information engineering from the University of Pisa, Pisa, Italy, in 2001 and 2005, respectively.

From 2002 through 2004, she was with the Department of Ingegneria dell'Informazione of the University of Pisa, where her research activity included modern spectral estimation and detection techniques for multichannel and multidata signal processing, with applications both in the field of synthetic aperture radar (SAR) interferometry and radar surveillance. From April 2004 to September 2004, she was Visiting Research Scholar at the Karlstad University, Sweden. From 2005 to 2007, she worked at Alenia Space, Rome, Italy, with the validation/certification of COSMO-SkyMed SAR products. Since 2007, she has been with the Microwaves and Radar Institute of the German Aerospace Center (DLR), Oberpfaffenhofen, Germany, where her scientific work has been focusing on innovative multichannel spaceborne SAR systems with digital beamforming capability, novel advanced operational modes for high-resolution wide-swath SAR imaging, and SAR imaging performance analysis. She is author or coauthor of more than 50 refereed journal and conference papers.



Gerhard Krieger (M'04-SM'09-F'13) received the Dipl.-Ing. (M.S.) and Dr.-Ing. (Ph.D.) (Hons.) degrees in electrical and communication engineering from the Technical University of Munich, Germany, in 1992 and 1999, respectively.

From 1992 to 1999, he was with the Ludwig Maximilians University, Munich, where he conducted multidisciplinary research on neuronal modeling and nonlinear information processing in biological and technical vision systems. Since 1999, he has been with the Microwaves and Radar Institute of the German Aerospace Center (DLR), Oberpfaffenhofen, Germany, where he started as a research associate developing signal processing algorithms for a novel forward-looking radar system employing digital beamforming on receive. From 2001 to 2007, he led the New SAR Missions Group which pioneered the development of advanced bistatic and multistatic radar systems, such as TanDEM-X, as well as innovative multichannel SAR techniques and algorithms for high-resolution wide-swath SAR imaging. Since 2008, he has been the Head of the Radar Concepts Department which hosts about 40 scientists focusing on new SAR techniques, missions and applications. He has been serving as Mission Engineer for TanDEM-X and he made also major contributions to the development of the Tandem-L mission concept, where he led the Phase-0 and Phase-A studies. Since 2019, he holds also professorship at the Friedrich-Alexander-University Erlangen, Germany. Gerhard Krieger is author or co-author of more than 100 peer-reviewed journal papers, 9 invited book chapters, more than 400 conference papers, and more than 20 patents.

Prof. Krieger has been an Associate Editor for the IEEE Transactions on Geoscience and Remote Sensing since 2012. In 2014, he served as the Technical Program Chair for the European Conference on Synthetic Aperture Radar and as a Guest Editor for the IEEE Journal of Selected Topics in Applied Earth Observations and Remote Sensing. He received several national and international awards, including two Best Paper Awards at the European Conference on Synthetic Aperture Radar, two Transactions Prize Paper Awards of the IEEE Geoscience and Remote Sensing Society, and the W.R.G. Baker Prize Paper Award from the IEEE Board of Directors.



David Lind received the M.Sc. degree in engineering physics from the Lund University, Lund, Sweden, in 2021. During 2020 was a master's thesis student at the Microwaves and Radar Institute of the German Aerospace Center, where he worked within the SAR field.

He is currently working for Spacemetric AB, Sollentuna, Sweden, with software development for remote sensing applications.